J. Anat. (2001) **198**, pp. 537–554, with 8 figures Printed in the United Kingdom

Investigation of feline brain anatomy for the detection of cortical spreading depression with magnetic resonance imaging

J. M. SMITH[1,2]*, M. F. JAMES[3]*, K. H. J. BOCKHORST[2]†, M. I. SMITH[3], D. P. BRADLEY[1,2], N. G. PAPADAKIS[1,2], T. A. CARPENTER[2]‡, A. A. PARSONS[3], R. A. LESLIE[3], L. D. HALL[2] AND C. L.-H. HUANG[1]

[1] *Physiological Laboratory, University of Cambridge,* [2] *Herchel Smith Laboratory for Medicinal Chemistry, University of Cambridge School of Clinical Medicine, Cambridge, and* [3] *Neuroscience Research, SmithKline Beecham Pharmaceuticals, Harlow, UK*

(*Accepted 21 November 2000*)

ABSTRACT

Cortical spreading depression (CSD) and peri-infarct depolarisation (PID) are related phenomena that have been associated with the human clinical syndromes of migraine (CSD), head injury and stroke (PID). Nevertheless the existence of CSD in man remains controversial, despite the detection of this phenomenon in the brains of most, if not all, other animal species investigated. This failure to unambiguously detect CSD clinically may be at least partly due to the anatomically complex, gyrencephalic structure of the human brain. This study was designed to establish conditions for the study of CSD in the brain of a gyrencephalic species using the noninvasive technique of magnetic resonance imaging (MRI). The 3-dimensional (3D) gyrencephalic anatomy of the cat brain was examined to determine the imaging conditions necessary to detect CSD events. Orthogonal transverse, sagittal and horizontal T_1-weighted image slices showed that the marginal and suprasylvian gyri were the most appropriate cortical structures to study CSD. This was in view of (1) their simple geometry: (2) their lengthy extent of grey matter orientated rostrocaudally in the cortex: (3) their separation by a sulcus across which CSD spread could be studied and (4) the discontinuity in the grey matter in these regions between the right and left hemispheres dorsal to the corpus callosum. The structure suggested by the T_1-weighted images was corroborated by systematic diffusion tensor imaging to map the fractional anisotropy and diffusion trace. Thus a single horizontal image plane could visualise the neighbouring suprasylvian and marginal gyri of both cerebral hemispheres, whereas its complex shape and position ruled out the ectosylvian gyrus for CSD studies. With the horizontal imaging plane, CSD events were reproducibly detected by animating successive diffusion-weighted MR images following local KCl stimulation of the cortical surface. In single image frames, CSD detection and characterisation required image subtraction or statistical mapping methods that, nevertheless, yielded concordant results. In repeat experiments, CSD events were qualitatively similar in appearance whether elicited by sustained or transient KCl applications. Our experimental approach thus successfully describes cat brain anatomy in vivo, and elucidates the necessary conditions for the application of MRI methods to detect CSD propagation.

Key words: Cat brain; cortical spreading depression; peri-infarct depolarisation.

Correspondence to Dr C. L.-H. Huang, Physiological Laboratory, University of Cambridge, Downing Street, Cambridge, CB2 3EG, UK: e-mail: clh11@cam.ac.uk

* Equal contributors to this paper.

† Present address: Universität Bremen, FBII, Instrumetelle Analytik, Postfach 330440, 28334 Bremen, Germany.

‡ Present address: Wolfson Brain Imaging Centre, University of Cambridge, Box 65 Addenbrooke's Hospital, Hills Road, Cambridge, CB2 2QQ, UK.

INTRODUCTION

The cat brain is a commonly used experimental model partly because this carnivore species has a complex gyrencephalic brain that resembles the human brain with its folded cerebral cortex. This neuroanatomical feature is absent in most other common experimental animals including rodents and even small primates such as the marmoset. Apart from this gross anatomical difference, some evidence suggests that there are also functional differences between gyrencephalic and lissencephalic brains. An example is the relative presence or absence of cortical spreading depression (CSD) and the related phenomenon peri-infarct depolarisation (PID).

Such differences are important because CSD is thought to be fundamental to the development of aura in migraine (Lauritzen, 1994), and PID to underly the expansion of the focal injury in stroke and head injury (Sramka et al. 1977; Back et al. 1994; Hossmann, 1996; Mayevsky et al. 1996). CSD wave propagation is associated with an ion redistribution across cell membranes in the affected regions, with a net cellular potassium efflux and corresponding sodium, chloride and calcium influx (Nicholson & Kraig, 1981). Such alterations in ionic homeostasis are thought to drive a net water influx into glia and neurons leading to cell swelling (Higashida et al. 1974). This decreases the apparent diffusion coefficient (ADC) of cerebral water over different cellular compartments of brain tissue, as has already been detected in rats using diffusion-weighted magnetic resonance imaging (DW-MRI) (Latour et al. 1994; Hasegawa et al. 1995; Rother et al. 1996; de Crespigny et al. 1998). However, if functional differences between anatomical brain types exist, then the choice of animal species for study of CSD is of significant concern. Gyrencephalic species have in fact been demonstrated to resist the initiation of CSD better than lissencephalic species (Marshall, 1959; Bures et al. 1974). Thus in contrast to the case in rodents, CSD initiation in the cat may be inhibited by some inhalational anaesthetics (Saito et al. 1995; Piper & Lambert, 1996) that may uncouple astrocytic gap junctions (Mantz et al. 1993). Some cytological differences between the 2 types of brain may partially explain this: in gyrencephalic species the ratio of glial:neuronal cells is greater (Tower & Young, 1973); glia may protect against CSD initiation (Gardner-Medwin, 1981; Szerb, 1991; Largo et al. 1997). Thus the complex nature of the cat brain makes it appropriate as an experimental model for such human neurological conditions.

Detailed information about cat brain anatomy is difficult to obtain. The standard anatomical atlases (Snider & Niemer, 1970; Berman & Jones, 1982) are based on histological sections and do not focus on cerebral surface anatomy. Even published material that does describe some 3D anatomy of the cat brain (e.g. Crouch, 1969) is based on postmortem dissection rather than in vivo examination. We have previously shown that CSD can be detected in the cat brain using MRI (James et al. 1999). That study defined an imaging protocol used to detect CSD together with some preliminary results, but we did not include a detailed analysis of the cat brain anatomy, as investigated in vivo, or develop analytical methods that would enable the systematic detection and characterisation of CSD.

The present experiments were thus designed to provide a detailed description of the surface gross anatomy of the cat brain as studied in vivo by MRI. From this, we derived appropriate imaging planes. We then explored the further conditions under which the spatiotemporal spread of CSD over the cortical surface of the cat brain might be detected and characterised with diffusion-weighted (DW)-MRI. We demonstrated these conditions to be appropriate for stable imaging of CSD propagation over considerably longer periods than used in earlier studies of CSD (Gardner-Medwin et al. 1994; Latour et al. 1994; de Crespigny et al. 1998). The long-lasting and injectable α-chloralose rather than gaseous halothane was used as anaesthetic: the latter agent is known to quench the CSD phenomenon (Saito et al. 1995; Piper & Lambert, 1996). By exploring systematically the conditions under which CSD events in the gyrencephalic brain of the cat might be detected using MRI, these studies helped establish some of the necessary conditions required for the noninvasive imaging of CSD in the human brain.

METHODS

Animal preparation

The experimental work was ethically approved by the SmithKline Beecham Procedures Review Panel and complied with the Animals (Scientific Procedures) Act 1986. Anaesthesia of fasted female cats (2.5–3.5 kg) was induced with 4–5% halothane and maintained with an initial dose of α-chloralose (30 mg/ml solution; approximately 100 mg/kg i.v.) administered through the cephalic vein. Supplementary doses of α-chloralose were given through the femoral vein cannula when indicated by the depth and stability of anaesthesia as monitored by a continuous blood pressure recording. As α-chloralose is a long-lasting

and stable anaesthetic, this typically involved only 1–2 further supplementary doses (each 2 ml giving a total dose of 140–160 mg/kg) during the course of the experiments. The cats were killed without recovery at the end of each experiment with a lethal injection of sodium pentobarbitone, in accordance with Schedule I euthanasia. Animals were ventilated mechanically (20–24 ml at 30 strokes/min) and their core temperature monitored by a rectal probe and maintained at 37 °C with a homeothermic blanket. Anaesthetic was administered through femoral vein cannulae whilst blood pressure and blood gases were monitored with femoral artery cannulae to confirm physiological stability throughout each experiment.

Craniotomies were performed in both orbital sinuses, which were then filled with agar (2 % in sterile saline) to reduce image susceptibility effects between brain and adjacent tissue which would induce severe artefacts in the diffusion-weighted fast echo-planar (DWEP) imaging technique used for CSD detection. For the purpose of collecting 3D MRI anatomical data and subsequent diffusion tensor images (DTI), the head of the animal was securely positioned within a 9.5 cm quadrature bird-cage MRI radiofrequency probe. In contrast, for those experiments in which CSD was to be induced, further surgical procedures were performed as modified from previous studies (Read et al. 1997). A second craniotomy with durectomy $\sim$ 1 cm lateral to the midline and 1.5 cm posterior to the bregma exposed the surface of the left suprasylvian gyrus (SG) for KCl application. For obtaining diffusion weighted MRI scans, a plastic-coated silver-wire surface coil (diameter 4 cm) was bonded symmetrically to the skull; this arrangement ensured a good filling factor and hence a good signal-to-noise ratio.

CSD was induced in 10 animals using KCl, which was applied using one of the following techniques in any given experiment: solid KCl (0.5 mmol) was carefully applied to the brain surface in 7 animals for the experimental duration, a technique shown reliably to initiate CSD (James et al. 1999). Alternatively, saturated KCl (3 M) in 2 % agar gel was applied to the brain surface from a delivery cannula for a 10 min period before being carefully retracted from the cortical surface in 3 animals. Dehydration of the cortical surface and dispersion of the KCl was prevented by forming a well flooded with mineral oil. Physiological variables were maintained stable throughout the experiment: blood pressure was continuously monitored to give values around (systolic/diastolic) $117.3/59 \pm 1.43/1.04$ mm Hg (mean $\pm$ S.E.M.). In a typical experiment, blood gases were first measured after the animal had been transferred onto the α-chloralose anaesthesia and mechanical ventilation had been established for 30–60 min early in the experimental proceedings. The measurements were then repeated just after the animal was placed in the magnet, and again just before acquisition of DWI–CSD data following animal positioning and the anatomical scans. They were then measured again at the end of the runs. It was not possible to conduct such measurements during data acquisition itself without disrupting the long periods of continuous data sampling that the experiments entailed. Typical arterial blood gas values that were obtained were pH 7.3 ± 0.01, PCO_2 31.8 ± 1.02 mm Hg, and PO_2 102.5 ± 13.08 mm Hg.

Image acquisition

Images were acquired using a whole body, 2.0 T super-conducting magnet (Oxford Magnet Technology, UK) driven by a MSL 400 console that ran Tomikon imaging software (version 890601) (Bruker Medizin Technik GmbH, Karlsruhe, Germany). The gradient set was 20.5 cm in diameter and of Maxwell–Golay design. A 9.5 cm diameter quadrature bird-cage probe (transmit and receive) was used to acquire 3D anatomical data. The 14 cm diameter sine-space transmit resonator used for diffusion weighted image acquisition incorporated a purpose built head-holder and animal tray. Positioning of the head within the magnet was checked by acquiring fast gradient echo (GE) images in the parasagittal plane (repeat time (TR) 100 ms, echo-time (TE) 10 ms, flip angle 60°, image matrix 128×256, and field of view (FoV) 10 cm).

The *anatomical study* acquired high-resolution 3D images encompassing the entire brain using a 3D spoiled gradient-echo (SPGR) imaging sequence (FoV $8 \times 8 \times 8$ cm, image matrix: $256 \times 256 \times 128$ (x,y,z), TR 35 ms, TE 7.5 ms), using the quadrature bird-cage probe. *Diffusion tensor imaging* (DTI) then studied the structure of the feline brain further (Basser et al. 1994) through providing complete directional descriptions of the self-diffusion properties of water caused by tissue structure (such as diffusion restrictions of the cellular water due to myelin sheaths in white matter). Measurement of the symmetric 3×3 self-diffusion tensor on a pixel by pixel basis allowed calculation of indices of anisotropy (Basser & Pierpaoli, 1996) that reflect the anisotropy of water diffusion in turn related to the architectural and structural coherence within each tissue pixel. Furthermore, the trace of the diffusion tensor (calculated as the mean of the 3

diagonal tensor elements) (Basser et al. 1994) reflects the mean water diffusivity within the tissue, without directional information; this is expected to be relatively uniform within healthy cerebral matter (Basser & Pierpaoli, 1996).

The DW interleaved echo-planar imaging (Papadakis et al. 1999) acquired 5 contiguous horizontal image slices with FoV 9 cm and slice thickness 4 mm and 4 interleaves per image. The image matrix was 128×128, symmetrically zero-filled to 256×256, with TE 82.5 ms. The duration (δ) of the DW gradient pulses, spaced (Δ) 43.5 ms apart, was 8.5 ms. DW acquisitions were performed along 24 noncollinear gradient directions using a single b-value of 1570 s mm^{-2}. Imaging with partial (62.5%) k-space coverage was performed. Use of ECG-gating acquisitions (Turner et al. 1990) and a navigator echo in the read direction (Anderson & Gore, 1994) minimised brain pulsation artefacts between interleaves. The repetition time (TR) was set to 5 R-R intervals of the ECG signal (TR = 1.875 s), acquiring data from one slice per RR interval. Two 'dummy' scans were performed to bring signal from long T1-components such as cerebrospinal fluid to the steady-state, thus avoiding ghosting artefacts. The sequence of the imaging gradients was designed so that they were rephased as soon as possible after their application so that their contribution to the B-matrix was negligible (Matiello et al. 1997). Automated shimming (Webb & Macovski, 1990) prior to DW-EPI optimised static field homogeneity over the regions of interest.

Time-lapse DWI studies

To detect CSD propagation, horizontal diffusion weighted echo-planar (DWEP) images were acquired using a repeated single shot spin echo imaging sequence (effective TR 7.5 s, TE 70 ms, 62.5% k-space acquisition using a 64×64 matrix symmetrically zero-filled at reconstruction to yield a 128×128 image with pixel dimension 0.39 mm, slice thickness 3 mm and FoV 5 cm) using the sine-space transmit resonator coil. Time-lapse DWI were acquired repeatedly in loops, each loop taking 14 s, prior to and following KCl application. Low (low-b) and high (high-b) diffusion-weighted images were acquired alternately (b-factors 100 and 850 s mm^{-2} respectively, $\delta = 10$ ms, $\Delta = 39$ ms applied in the z direction) (Xing et al. 1997). Template images were acquired for each of the contrasts and used for phase correction during image reconstruction. DWEP images were recorded for about 30 min prior to the deposition of KCl (pre-KCl) and for ~ 60 min after stimulus application (post-KCl). Phantom data acquired prior to each experiment confirmed appropriate stability and image signal to noise ratio.

Image processing and analysis

Image reconstruction by Fourier transformation employed GNU/Debian Linux version 1.3 and in-house reconstruction software (CamRes, Herchel Smith Laboratory for Medicinal Chemistry, Cambridge, UK). Reconstructed 3D *anatomical data* were transferred to a Silicon graphics workstation running surface rendering software (Volren, Silicon Graphics, CA, USA). The 3D data set was first visualised as a series of 2D transverse image slices. A manual masking technique, in conjunction with thresholding, then displayed each slice without surrounding fascia. The resulting image set was then reconstituted back into a 3D data set that could be rotated into any position and resliced. The *DTI data* were processed pixelwise. The elements of the diffusion tensor and the baseline (zero DW) signal were fitted to all the DTI signals using a multivariate non–linear least-squares fitting routine (Press et al. 1992) applied to the sets of diffusion tensor equations (Basser et al. 1994). Maps of the fractional anisotropy (FA) (Basser & Pierpaoli, 1996) and of the trace of the diffusion tensor were derived from the 6 independent elements of the diffusion tensor.

Reconstructed *DWEP images* were analysed using in-house Interactive Data Language programs (IDL, Research Systems, Boulder, Colorado, USA). A brain image mask was created for each experiment by applying a median filter of 9 pixels and a threshold of 1.5 times the mean value of all the images that were obtained in the course of that experiment. Data excluded by this mask were ignored to reduce calculation times and to clarify data presentation. Each masked low-b image was combined both with its preceding and its following high-b image to derive maps of the apparent diffusion coefficient (ADC) with enhanced temporal resolution.

DWEP image analysis

Two differing methods of analysis were developed to detect and display propagating CSD activity. First, to reveal the changes in diffusion after KCl application, a preresponse reference high-b image obtained in the absence of any CSD was subtracted from the remaining post KCl high-b images. The resulting data were median-filtered and thresholded to isolate the hyperintense areas representing reduced diffusion. The hyperintense areas were colourcoded according

to the magnitude of the change and superimposed onto a reference image to illustrate CSD passage. Secondly, pixels with significantly different, more negative, ADC values were detected using running *t* tests. These performed pixel-by-pixel comparisons of successive pairs of ADC images against the remaining frames in the post-KCl time series, excluding the 2 images selected ($P < 0.05$, Bonferroni corrected). The result of each such *t* test was scaled to the interval [0, 15] and appropriately colour coded. The resulting maps that represented the value of *t* for each pixel were superimposed on the monochrome image that was calculated from the mean of all the images recorded at the high-b value in that particular time series. Both approaches to image analysis made it possible to visualise CSD wavefronts in stationary frames, which were otherwise only visible when a series of raw high-b images were viewed as a movie. Finally, such maps were superimposed upon the corresponding anatomical representations of the cortical slices in which ADC changes were investigated, in order to identify the anatomical region where such events took place.

RESULTS

Anatomy of the marginal, suprasylvian and ectosylvian gyri

Figure 1 displays the complex 3D surface anatomy of the cat brain in 3 orthogonal views with exterior surface rendering. The major external anatomical landmarks are identified (Crouch, 1969; Snider & Niemer, 1970; Berman & Jones, 1982): these guided the pilot studies which defined imaging planes appropriate for the functional experiments. The marginal, suprasylvian and ectosylvian gyri run rostrocaudally and are separated by sulci which contain large draining veins, in particular the superior sagittal sinus (not imaged with this pulse sequence). The marginal gyrus is the longest of the 3, but it is bounded by large vessels such as the sagittal sinus that impair surgical access. Fig. 1 indicates that the suprasylvian gyrus is most suitable for CSD initiation and imaging because, although situated somewhat laterally, it is relatively dorsally positioned, runs the length of the cortex, and is bounded by vessels that do not severely hinder surgical manipulation. Furthermore, because gyri with continuous grey matter lie on either side of this gyrus, CSD initiation on the suprasylvian gyrus permits any propagation of CSD to this adjacent gyrus to be investigated. In contrast the ectosylvian gyrus is too lateral in position and too short for easy imaging access: it lies under the large temporalis muscle, making surgical access for CSD initiation more difficult.

Figure 2 displays T1-weighted transverse images of the cat brain that distinguish brain structures related to the marginal (M), suprasylvian (S) and ectosylvian (E) gyri respectively. The accompanying pilot image shows the location of the transverse slices on the 3D image. There is good contrast between the grey and white matter and good anatomical detail. These images confirm the continuity of both grey and white matter along the length of the marginal and suprasylvian gyri. The grey matter is also continuous between adjacent gyri although it is considerably thinner (by $\sim 50\%$) at the bases of the sulci compared with at the gyral apices. The grey matter of the 2 hemispheres is not contiguous over the dorsal surface of the corpus callosum. Fibre tracts ascend ventrodorsally from the internal capsule and the corpus callosum and branch to each of the gyri, much as in the human brain. However, each transverse section displays a limited region of grey matter only and thus images in this orientation present analysis of CSD propagation along the length of the gyrus. Figure 3 illustrates the complementary T1-weighted images in the sagittal planes. These reveal the marginal and suprasylvian gyri more fully but any given slice provides an image of only one, not both these gyri. The cingulate gyrus, adjacent to the central sulcus and deep to the marginal gyrus, is clearly seen.

Use of tangential rather than perpendicular imaging planes

The MRI image slices in Figures 2 and 3 made it possible to define horizontal planes (x–z dimensions in the magnet) that would clearly allow imaging of the marginal and suprasylvian gyri. Figure 4 provides the appropriate series of T1-weighted horizontal images that were obtained at 1.07 mm intervals. Frames (A) and (B) were placed at the level of the olfactory bulbs and the corpus callosum respectively; these anatomical landmarks were used to identify the necessary baseline anatomical slices. Images (E–H) capture the ectosylvian gyri although only small sections of them were visible owing to their complex folded shape. The more superior image slices (I–K) captured usable lengths of both the marginal and suprasylvian gyri suitable for CSD studies. As the horizontal images ascend dorsally, the white matter rami that innervate the grey matter of the individual gyri could be observed to divide and separate. At the cortical surface the gyri were completely distinguishable from each other.

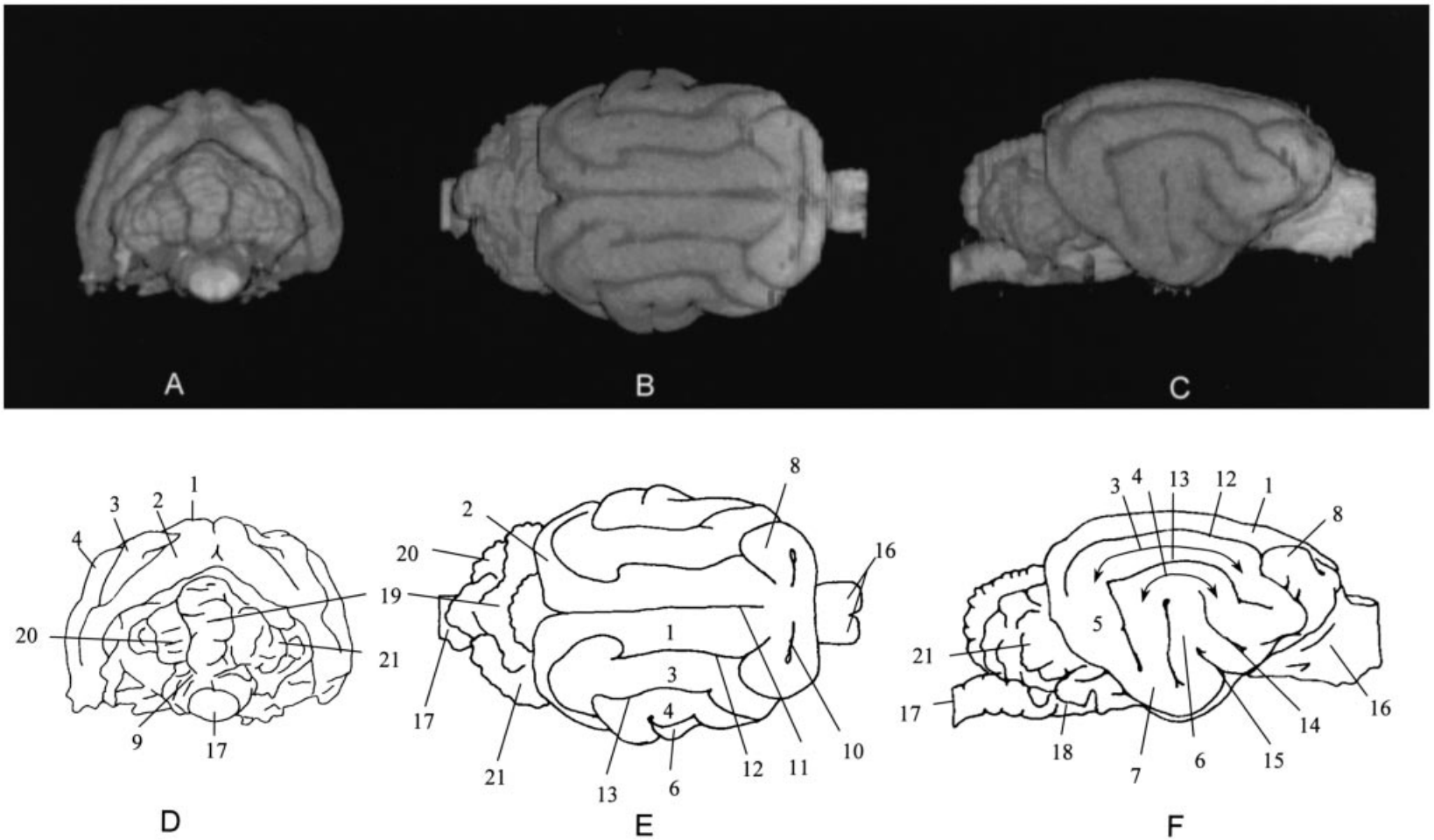

Fig. 1. The cat brain rendered 3-dimensionally. Caudal (*A*), dorsal (*B*) and lateral (*C*) views show the major cerebral structures, including the cortical hemispheres, the cerebellum and the rhombencephalon (panels *D–F* respectively). The 3 major gyri—the marginal (1), suprasylvian (3) and ectosylvian (4) in panels *D–F*—are clearly illustrated in the line drawings, along with other major structures. *Cerebrum*: (1) marginal gyrus, (2) occipital gyrus, (3) suprasylvian or ectomarginal gyrus, (4) ectosylvian gyrus, (5) composite gyrus, (6) anterior sylvian gyrus, (7) sylvian gyrus, (8) coronal gyrus, (9) piriform lobe, (10) cruciate sulcus, (11) central sulcus containing the suprasagittal sinus, (12) lateral sulcus, (13) suprasylvian sulcus, (14) anterior sulcus, (15) sylvian fissure, (16) olfactory lobes, (17) spinal cord, (18) medulla oblongata. *Cerebellum*: (19) declive, (20) paramedian lobule, (21) ansiform lobule.

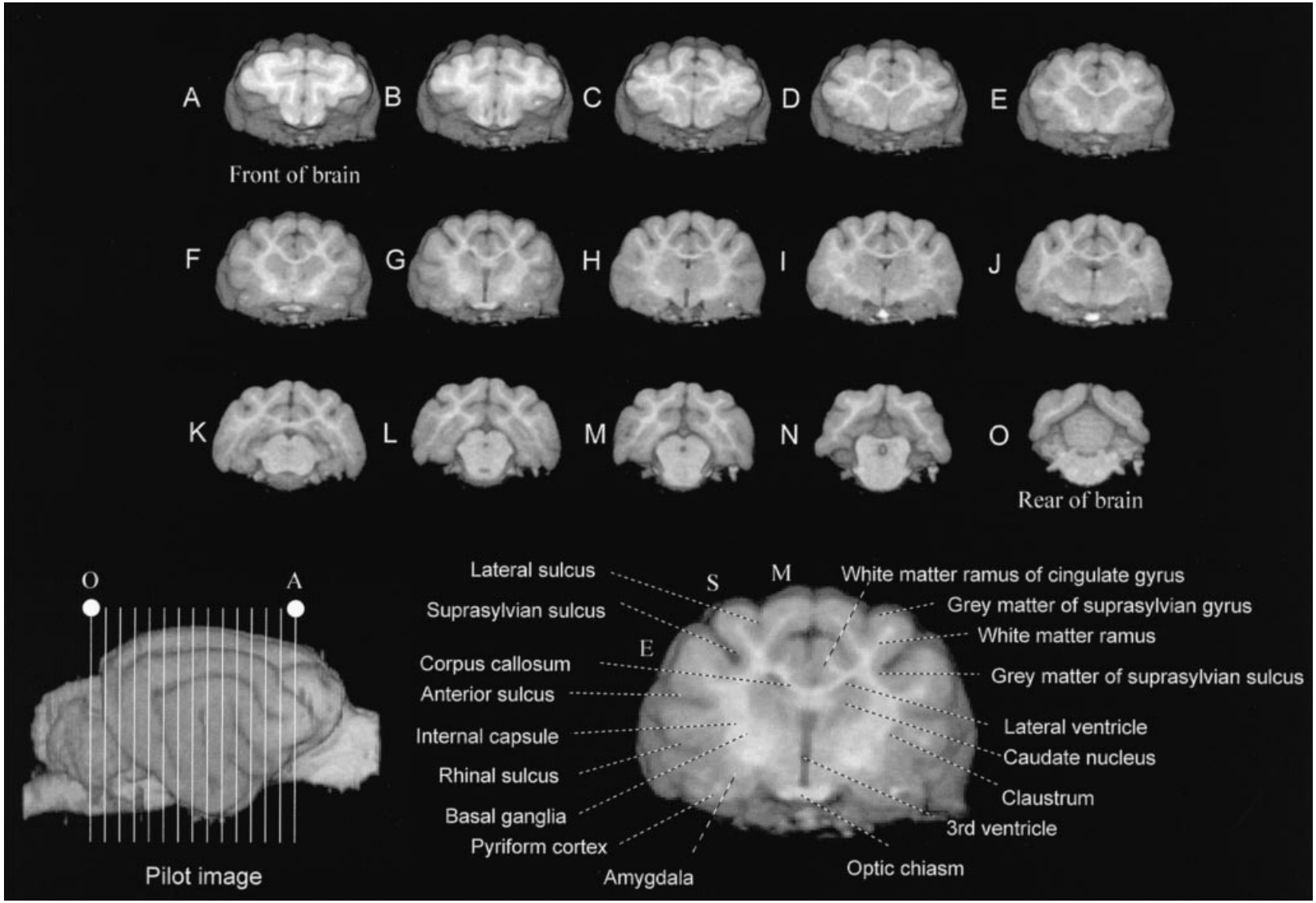

Fig. 2. The cat brain in transverse section. (A–O) Successive transverse sections running in a rostrocaudal direction as indicated in the pilot image (bottom left). Bottom right: Enlargement of image G identifying the marginal (M), suprasylvian (S), and ectosylvian gyri (E), and other details of the anatomy. The horizontal slice selected for CSD imaging included the grey matter of the marginal and suprasylvian gyri. The grey matter is continuous across each hemisphere, although at the sulcal bases it is much thinner than at the gyral apices. The hemispheres are linked by the corpus callosum and grey matter ventral to it. Grey matter does not bridge the hemispheres dorsal to the corpus callosum. Only white matter connects the cerebral hemispheres. (Slice thickness, 0.6 mm: inter–slice distance, 2 mm).

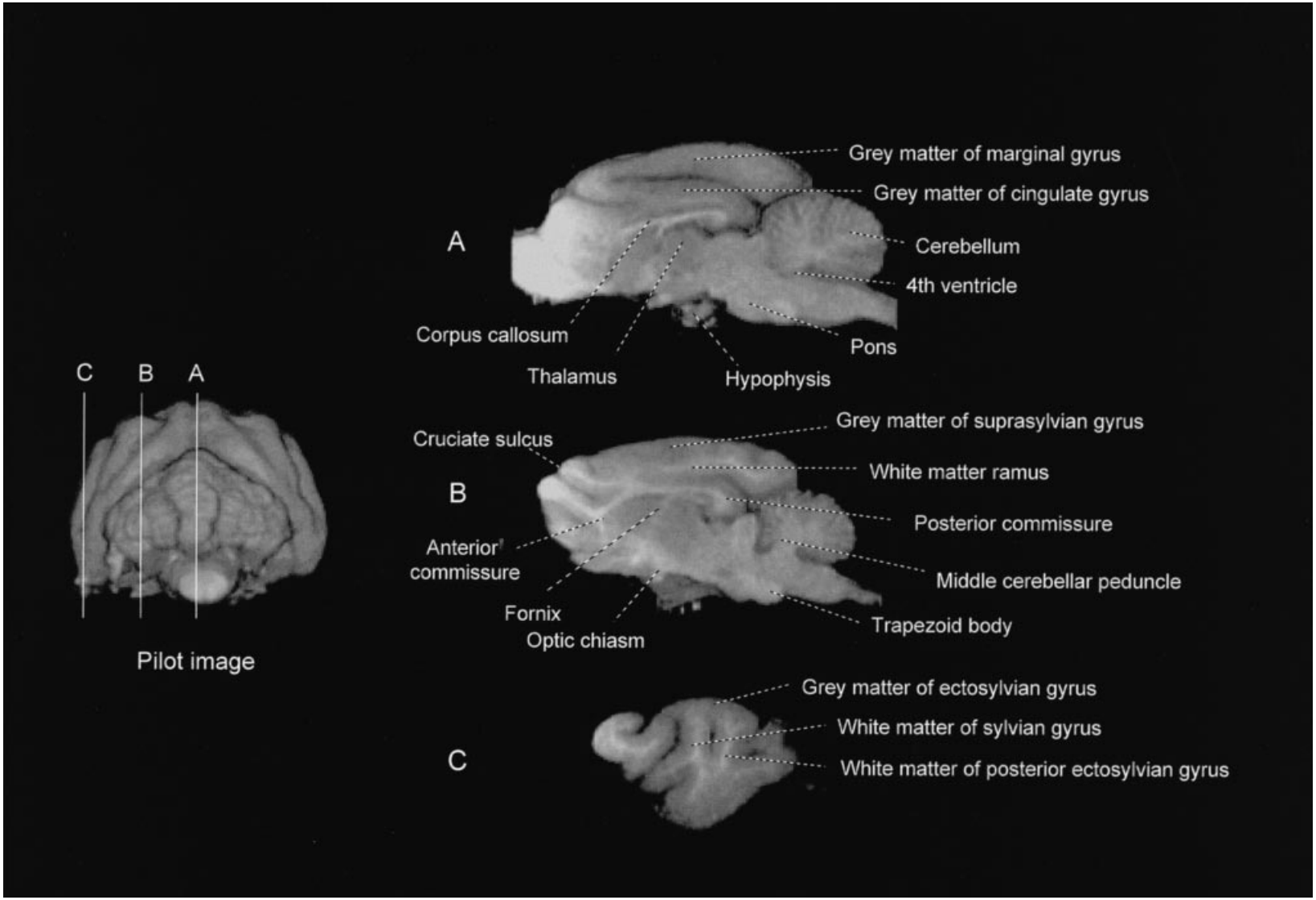

Fig. 3. The cat brain in sagittal section. Longitudinal sections of the cat brain through successive lateral planes demonstrating the long–axis of the marginal (*A*), suprasylvian (*B*) and ectosylvian gyri (*C*) and other details of the anatomy. The pilot image show the positions of the sagittal image slices (slice thickness = 0.3 mm and inter–slice distance = 5 mm).

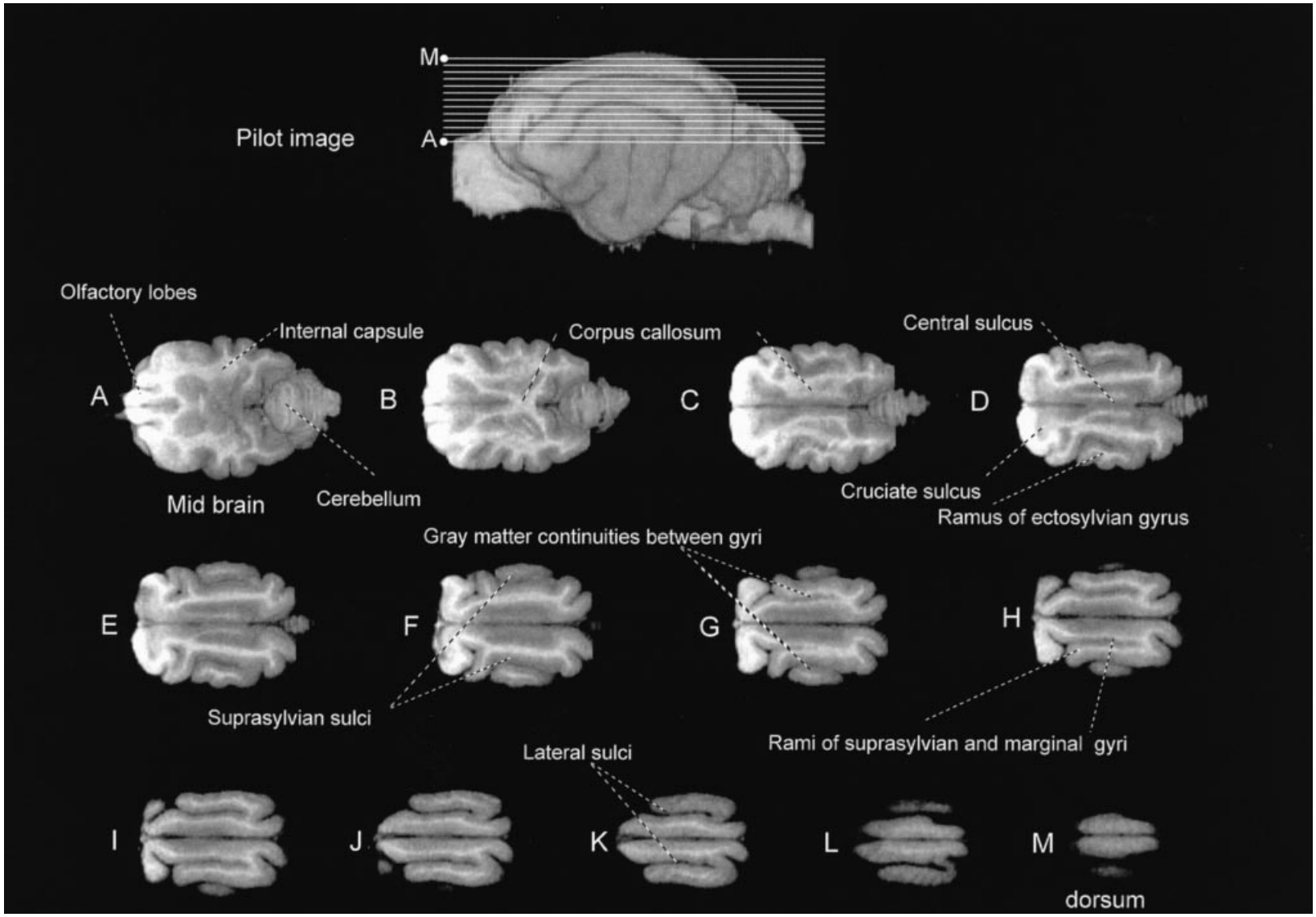

Fig. 4. The cat brain in horizontal section. The images ascend ventrodorsally from the level of the olfactory bulb (*A*) and corpus callosum (*B*). Frames C–M show how the white matter rami that penetrate the gyri arise from the corpus callosum and the internal capsule. The horizontal image adopted for CSD investigation incorporated slices K–M. The pilot image shows the positions of the horizontal image slices (slice thickness = 0.3 mm and inter–slice distance = 1.07 mm).

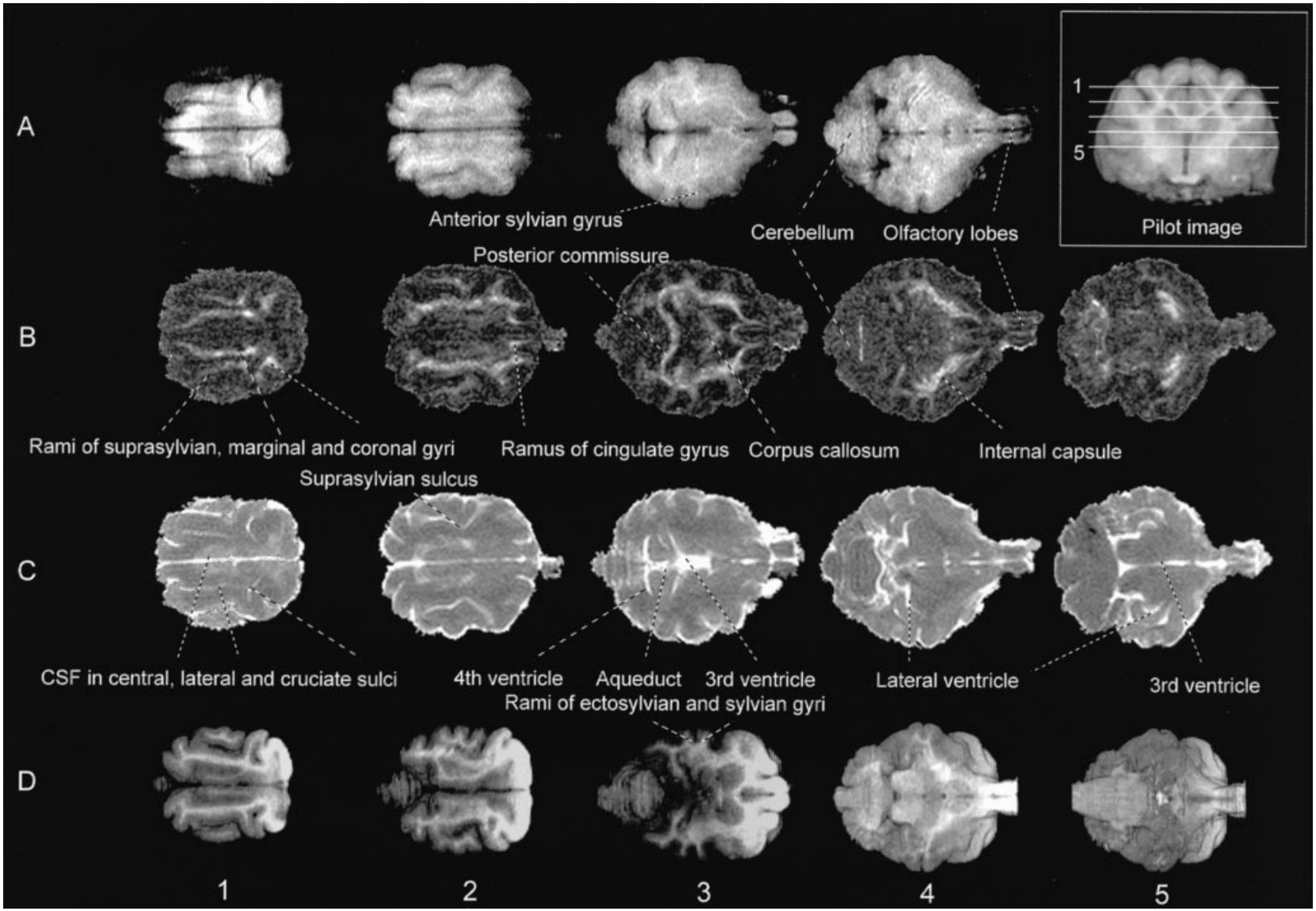

Fig. 5. Diffusion tensor images of the in vivo cat brain. Contiguous horizontal T1-weighted (*A*), fractional anisotropy (*B*) and diffusion trace (*C*) images descending dorsoventrally (planes 1–5) from the cortical surface, and matching T1-weighted 3D image slices (*D*) for anatomical comparison (left, rostral; right, caudal). Fractional anisotropy maps (*B*) demonstrate the directional constraints placed by the tissue architecture on cerebral water diffusivity: shown in dark are regions where cerebral water diffusion is randomly directed (grey matter) whereas bright areas indicate high anisotropy due to orientation of myelinated fibre bundles. In contrast, the diffusion trace (*C*) numerically maps the apparent diffusion coefficient of cerebral water without a directional component (thus there is little anatomical differentiation); bright areas have high diffusivity and correspond to cerebrospinal fluid. The pilot image shows the approximate positions of the horizontal images (slice thickness = 4 mm for *A*-*C*, 0.3 mm for *D*; fractional anisotropy images scaled 0–1; trace images scaled from $0–1.5 \times 10^{-3}$ s mm^{-2}).

To confirm that the T1-weighted images (Figs 1–4) correctly demarcated the cortical white and grey matter, diffusion tensor imaging was carried out to map the fractional anisotropy (FA), scaled from 0 to 1.0, and diffusion trace, scaled from 0 to 1.5×10^{-3} mm^2 s^{-1}, of the cerebrum. Figure 5 shows 5 contiguous horizontal slices with their approximate ventrodorsal locations indicated on the pilot image inset. The FA maps (Fig. 5*B*) show a high degree of order in the white matter tracts, including the internal capsule and its ramifications into the dorsal cortical gyri. A comparison of Figures 5*B*, *D* confirms that the T1-weighted contrast does correctly identify the white and grey matter tracts of the dorsal cerebrum. However, while the olfactory lobes appear bright in the T1-weighted images, their anisotropy is relatively low, showing that the contrast sources in these images are not identical. The diffusion trace images (Fig. 5*C*) help to confirm the structural identification. Fig. 5*C* clarifies the distribution of cerebrospinal fluid in the dorsal sulci and in the ventricular network: the cerebral ventricular anatomy is especially difficult to discern even in the anatomical, T1-weighted images (Fig. 5*D*) that allow grey/white matter discrimination.

CSD selectively propagates through the superficial cortical grey matter (Leao & Morrison, 1945; Ochs & Hunt, 1960) so the optimum experimental imaging plane must provide as complete a view of the CSD trajectory as possible. Taken together, the horizontal imaging planes shown in Figures 4 and 5 satisfy the criteria for detailed imaging studies of the CSD phenomenon. Thus (1) both the marginal and suprasylvian gyri are observed to be relatively broad, simple in geometry and to extend the length of the hemispheres; (2) the horizontal imaging plane captures the grey matter of individual gyri relatively selectively, and provides a sufficiently large view to permit CSD detection along the length of each gyrus; (3) the horizontal plane makes it possible to study CSD propagation between 2 neighbouring gyri; (4) it also provides symmetric brain images so that the contralateral side could act as a control, and (5) it excludes many other anatomical structures and thereby facilitates interpretation of DW-images.

In contrast, the brain curvature excluded the ectosylvian gyrus as a suitable structure for imaging in this respect. Its shape is too tortuous and it is relatively inaccessible for both surgical and experimental purposes because at this point the skull lies deep to the temporalis muscle. Transverse sections similar to those used in rodent imaging studies of CSD would only visualise a small proportion of the surface grey matter of the cat, although such sections do show the neighbouring gyri. The sagittal sections only permit the study of CSD in a single gyrus in a given section, and do not permit study of its spread to adjacent gyri or comparisons with the contralateral side.

Analytical methods to visualise CSD in MR images

Figure 6 displays typical results from application of different analysis methods to either the high-b DW-MRI or ADC map data obtained using the horizontal imaging plane. Because these are echo planar images (EPI), they are slightly distorted in comparison with the more slowly acquired anatomical GE images shown previously. Due to susceptibility effects at the interfaces between the brain tissue, the skull and air, DW–EPI also provides less anatomical contrast. Since the diffusion weighting was applied in the z-direction (left-right in Fig. 6, i.e. rostrocaudally) the gyral and sulcal anatomy is still discernible (sulci appear darker than the gyri on either side). The pale patches adjacent to the brain represent extracerebral tissue captured in the plane of the image slice. Despite the distortion of EPI, this technique allows rapid repetition of image acquisition; thus dynamic cerebral responses can be detected. Images were acquired in the $\sim$ 90 min period following the application of KCl stimuli used to induce CSD events. This time-period represents a considerably longer experimental interval than has been reported in previous investigations (Gardner-Medwin et al. 1994; Latour et al. 1994; de Crespigny et al. 1998).

Figure 6*A* shows a sequence of frames of selected high-b DW–EPI images. This technique is highly sensitive to ADC changes. The images were captured during the duration of a CSD wave as it moved over the hemisphere in which it was initiated but the images were not otherwise subjected to any form of statistical or signal analysis. Animation of successive high-b frames successfully allowed the qualitative visualisation of the spread of transient ADC changes along the gyri following KCl application. Such movies did not provide sufficient contrast to allow CSD events to be located clearly in individual frames. However, an inspection of the individual frames in Figure 6*A* does not reveal any obvious differences in signal intensity. These problems prompted explorations of specific analytical methods that would demonstrate significant ADC changes in single frames for detailed study, using both signal and statistical testing techniques.

Figure 6*B* shows the results of subtracting a single baseline image that was acquired prior to CSD activity, from the later high-b images. Regions of

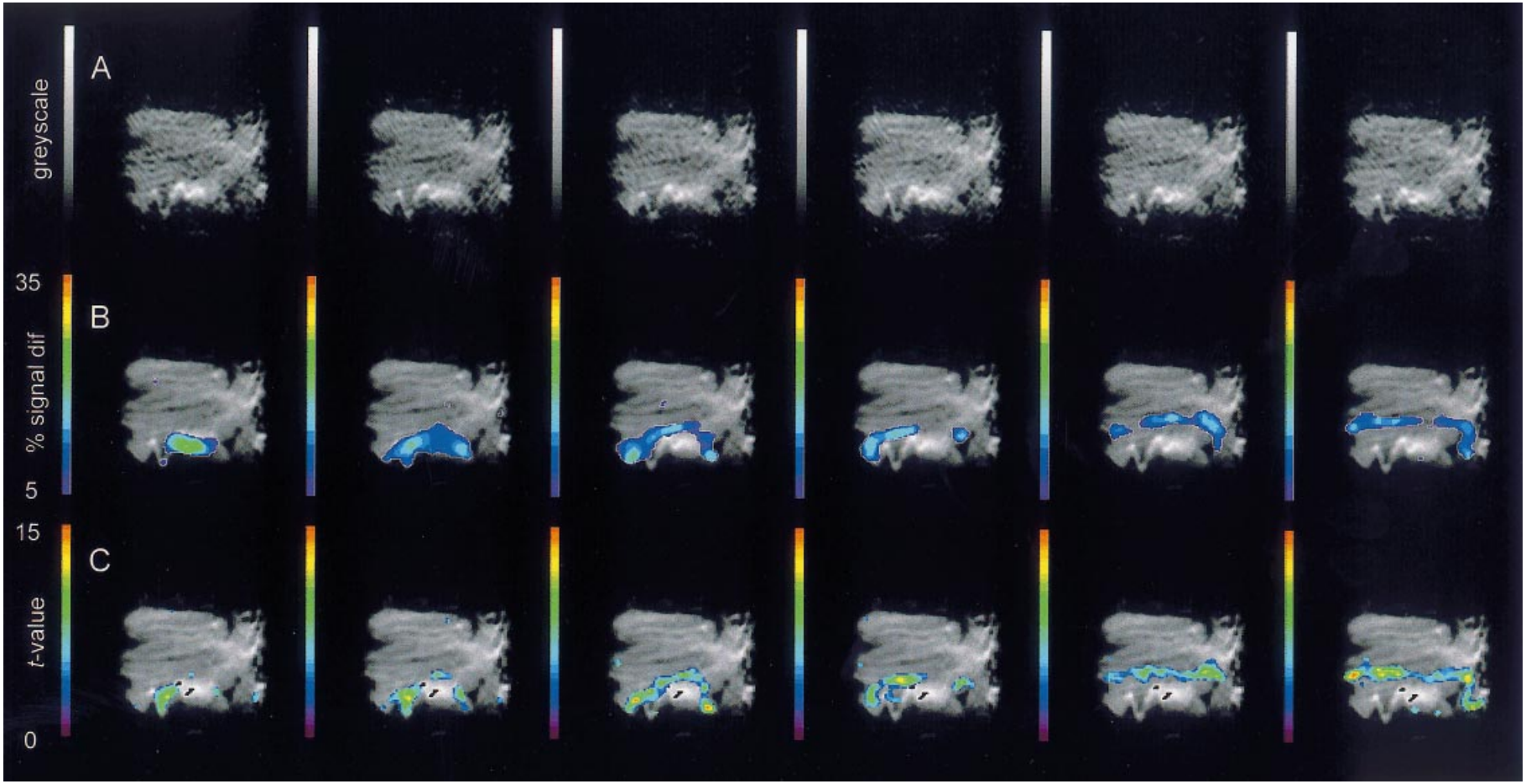

Fig. 6. The visualisation and analysis of propagating cortical spreading depression (CSD) events. Successive frames that represent high-b diffusion-weighted images: left, rostral; right, caudal; lower, left; upper, right. Field of view 5 cm. (*A*) Series of single shot, spin echo, echo planar high-b diffusion-weighted images obtained 1.4, 2.33, 3.27, 4.2, 5.6, and 6.53 min, respectively, after the initiation of the primary wave. The arbitrary grey scale was designed to maximise image contrast. (*B*) A series of subtraction images were then derived from a reference preresponse high-b image, subtracted from each of the post-KCl high-b images. These gave rise to the superimposed coloured overlays representing the resulting percentage signal differences at $t = 1.4$, 2.33, 3.27, 4.2, 5.6, and 6.53 min, respectively. The colour code varies from 5 to 35% of the reference level in each given pixel. In (*C*), the overlays are the results of the running t tests applied to ADC map data as described in the Methods. The colour scale represents t values between 0–15 for each individual pixel (see Methods and Results for details of statistical mapping). Frames represent $t = 1.46$, 2.39, 3.33, 4.26, 5.66, and 6.59 min after event initiation. Comparison of *B* with *C* shows that the subtractive method provides an exaggerated indication of the area affected by the CSD event. In the raw high-b images (*A*) the CSD event is not visible to the eye unless the frames are animated. Grey regions outside the brain are extracerebral tissues within the image slice.

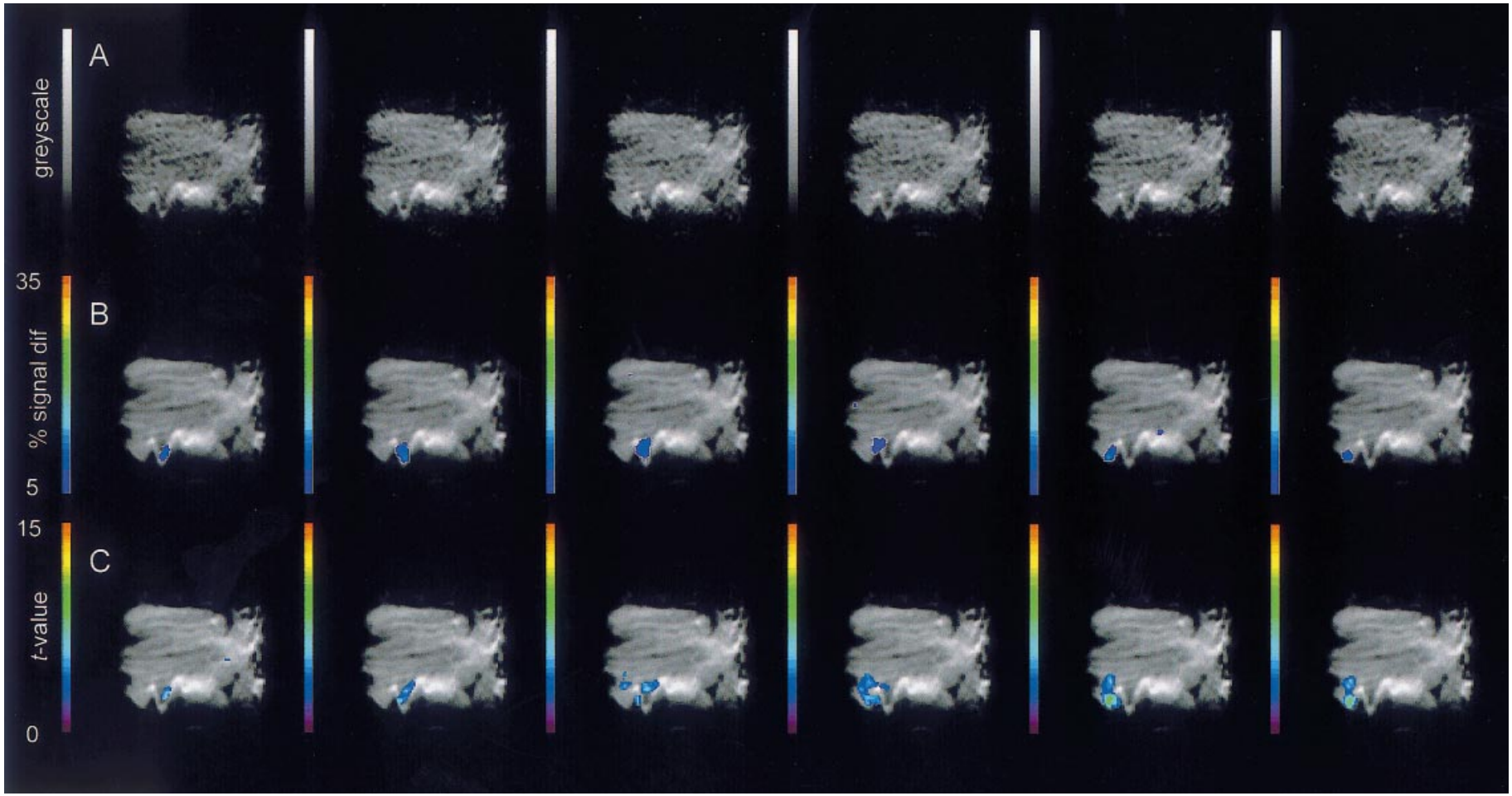

Fig. 7. Visualisation and analysis of secondary CSD events. Successive series of frames representing the different methods of image visualisation and analysis as described in Fig. 6, applied to a secondary CSD event. Frames in rows (*A*) and (*B*) were taken 0.47, 1.4, 1.87, 2.33, 3.27 and 3.73 min, respectively, after the start of the secondary wave. Frames in row (*C*) were at times 0.53, 1.46, 1.93, 2.39, 3.33 and 3.79 min, respectively. As in Fig. 5, the passage of the CSD event is invisible in individual high-b frames (*A*). The subtractive method (*B*) provides an exaggerated indication of the area affected by the CSD in comparison with the statistical method (*C*). Secondary events were constrained in area and extent compared with primary events.

reduced diffusion are colour coded according to the magnitude of the change (5–35%) and superimposed onto a reference image. Although this subtraction method precluded a representation of absolute as opposed to relative intensities, it did reveal a comparatively large area of increased signal representing reduced diffusion which spreads from the point of KCl application on the suprasylvian gyrus, into the marginal gyrus (last 2 frames). In comparison with the movie of the frames in Figure 6*A*, the coloured areas in Figure 6*B* appeared to be more extensive than the changes observed in the movie, but the wave propagated across the cortical surface in a similar manner.

Finally, Figure 6*C* displays the results of image processing involving the statistical detection followed by mapping of the ADC changes. Mapping ADC values enabled a direct quantitative representation of the absolute value of ADC in individual pixels in contrast merely to offering qualititative intensity maps. Here, coloured overlays represent the value of *t* for each pixel, on the same baseline image as employed in Figure 6*B*. Since the computation combined each high-b image with its preceding and following low-b images, twice as many *t* test maps of ADC change were obtained. However, Figure 6*C* only shows those maps that correspond to the images in Figure 6*B*.

The maps in Figure 6*C* provided the closest representations of the size and propagation of the CSD wave front as observed in movies of Figure 6*A*, such waves were invisible in single frames. They suggest a more restricted extent of cortex affected by the wave at any given time compared to that suggested by the difference image (Fig. 6*B*). However, Figure 6*C* provides a statistically tested and objective measure of significant ADC change, which allowed a more stringent retrospective assessment of the individual pixels underlying the *t* value of each frame. Furthermore, the statistical technique employed determination of ADC values and these were obtained by combining high and comparably less noisy, low-b data sets. In contrast the difference images (Fig. 6*B*) were derived from a single subtraction of 2 intrinsically noisier high-b data sets, one obtained prior, and the other following CSD initiation, in which additionally the absolute magnitude of the changes were lost. Both methods of data analysis gave similar results in revealing the propagation of a concentric wave front of reduced ADC that moved over the cortex away from the site of KCl application. Thus the first CSD event initiated by KCl application progressively developed into an elliptical region of transiently reduced diffusibility crossing both the suprasylvian and marginal gyri. These changes in ADC were clearly confined to the hemisphere in which the KCl stimulus was applied. Such primary events covered up to 22.5 ± 3.27% (mean $\pm$ S.E.M.; n = 7) of the surface area of the suprasylvian gyrus over which they propagated at a velocity of 3.3 ± 0.75 mm min^{-1}, producing a depression in apparent diffusion coefficient of about 23%, to 76.9 ± 2.42% of its baseline value.

Figure 7 further illustrates the importance of the more sensitive statistical method of CSD detection. Following the initiation of the first CSD event, which spreads across the ipsilateral hemisphere surface, movies of the raw (high-b) images showed further events, but these were much more restricted in the cortical area involved. The difference images of subsequent wave propagations (Fig. 7*B*) similarly showed that they covered small circumscribed areas with a uniformly increased signal intensity. More detailed statistical analysis of the ADC maps revealed that these restricted regions of reduced diffusion more closely matched the waveforms of observed high-b movies. Thus these could change dynamically in extent and even divide, and could generate a greater range of signal variation than could the difference images. Thus secondary events appeared more fragmented and were markedly less widespread than the preceding primary waves; they were also often confined to the originating suprasylvian gyrus. Such *t* maps allowed an accurate determination of secondary waves and identified those regions affected by the CSD events that were initially observed in the raw DWI movies. The *t* mapping showed that these CSD events occurred secondarily to the large hemispheric primary events and were restricted anatomically and propagated with a slightly lower velocity. Up to 5 such secondary events could be counted over both the suprasylvian and marginal gyri in each experiment in the 20 min that followed the application of KCl. These covered more circumscribed areas of cortex (e.g. up to 7.9 ± 2.25%, of 5 events counted, of the visible surface area of the suprasylvian gyrus). They propagated with a velocity of 3.0 ± 0.68 mm min^{-1} and produced similar depressions in apparent diffusion coefficient to 79.0 ± 4.32% of its baseline value.

The effects of sustained and transient stimuli that induce CSD

The final experiments compared the results of using 2 different methods of KCl-stimulated CSD induction. Crystalline KCl (0.5 mM) was left on the cortical

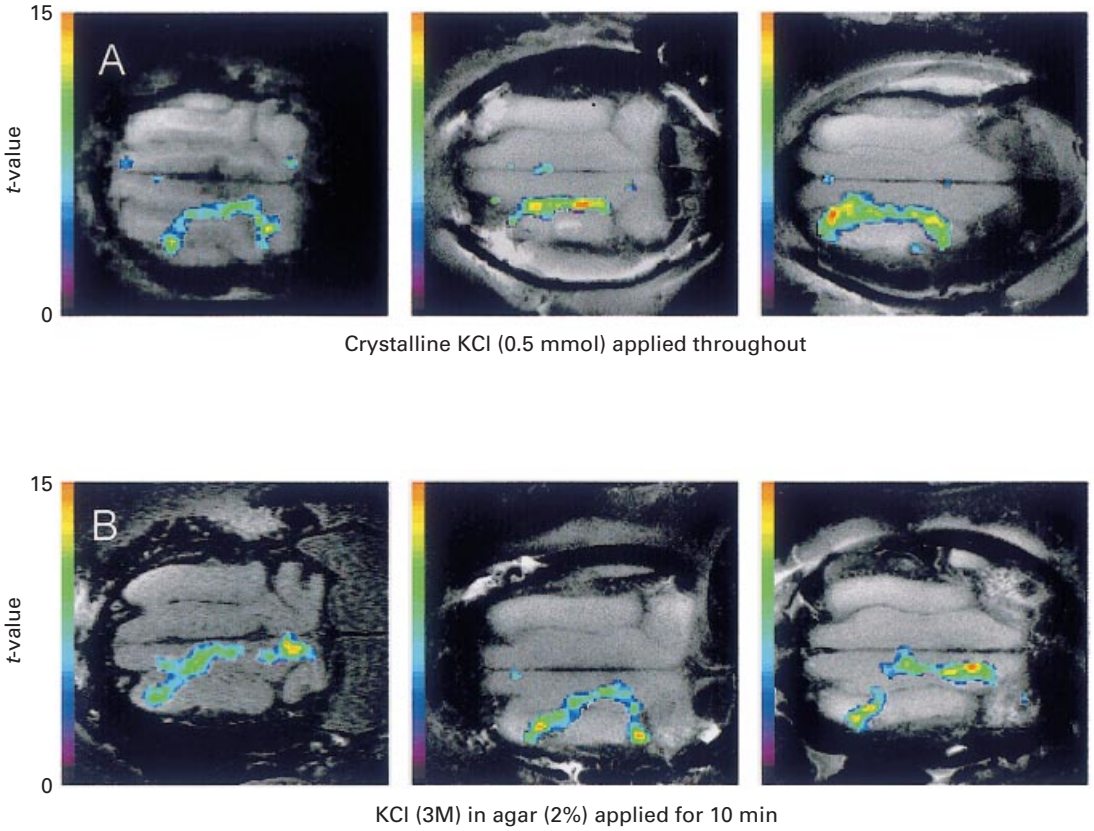

Fig. 8. A qualitative comparison of CSD events resulting from 2 methods of KCl application. Panel (*A*) displays, in 3 separate experiments, representative primary CSD events induced by a continuous, localised application of solid KCl (0.5 mmol) at the centre of the suprasylvian gyrus. (*B*) Similar CSD waves induced in 3 further experiments by the transient (10 min) application of KCl (3M) in agar. Events were statistically mapped onto the respective gradient-echo, horizontal brain images. The images represent a coherent, elliptical wave of reduced diffusion propagating across the marginal and suprasylvian gyri; the mode of KCl application appeared to make little qualitative difference to the nature of the event initiated. Field of view 5 cm.

surface to induce a sustained response (Fig. 8*A*). Alternatively, KCl (3 M) was applied in agar gel using a remote applicator; this was then removed after 10 min to provide a transient stimulus (Fig. 8*B*). Figure 8 additionally demonstrates the results of statistically mapping ADC changes from 6 different experiments onto anatomical images. Comparison of the images in Figure 8 furthermore confirms the reproducibility of the CSD wavefronts thus deduced. Such a mapping method was easily achieved using the imaging plane that was adopted here. Thus the latter covered a homogeneous, restricted region of brain that was exclusively directed at the gyri of interest and in which the boundaries of the EPI coincided with the anatomical limits of the tissue.

A hypothesis in which the CSD phenomenon requires the presence of sustained stimulation from its initiating focus would predict that transient stimulus applications would fail to give rise to spreading CSD waves. In contrast, a regenerative propagation that was triggered instead by already affected regions would predict comparable patterns of CSD spread following the successful initiation of such a wave. The features of CSD generation and propagation shown in Figure 8 are consistent with the latter hypothesis. Thus either method of CSD induction produced coherent elliptical shaped wavefronts that traversed the suprasylvian gyrus in which CSD was initiated, then subsequently crossed the marginal gyrus before reaching the midline. In both cases the waves failed to cross the midline from the cortical hemisphere on which they were induced. In both cases multiple secondary waves were observed.

Taken together, these observations indicate that CSD events, initiated by maintained or transient application of KCl, can be detected in the gyrencephalic feline brain using DWI. Because CSD has been detected in all animal species so far investigated, it seems inherently unlikely that the CSD phenomenon cannot also occur in man. Thus this study indicates that appropriate imaging and signal detection procedures are important for CSD detection and, we suggest, should facilitate the investigation of CSD in the human brain.

DISCUSSION

The experiments described here sought, firstly, to document the complex anatomy of the cat brain using structural MRI. The standard anatomical cat brain architecture is largely based on histological sections and focuses primarily on the cerebral nuclear anatomy (Crouch, 1969; Snider & Niemer, 1970; Berman & Jones, 1982). The detailed macroscopic understanding of the cat brain which emerged from the MRI studies was essential for the second aim of this work: the selection of image planes that included key gyral structures in which spreading CSD events would be consistently detectable. Such imaging planes had to be reproducible, making use of readily identifiable anatomical landmarks. Accordingly, a complete T1-weighted 3D MRI data set of the cat brain was obtained (Figs 1–4) which led to the adoption of a specific imaging plane for CSD investigations. The cerebral morphology discerned from the T1-weighted images were further examined using diffusion tensor imaging (Fig. 5). This clearly distinguishes the grey and white matter and the cerebral ventricular network and complemented and thus confirmed the information from the 3D images.

For CSD experiments (Figs 6–8), the horizontal imaging plane was adopted in order to visualise simultaneously the grey matter within the marginal and the suprasylvian gyri, as well as the sulci between them. This made it possible to detect not only the pattern of spread within a gyrus, but also between gyri, and allowed the contralateral hemisphere to act as an internal control. The latter confirmed that CSD waves did not cross the midline between hemispheres where the grey matter is discontinuous dorsal to the corpus callosum. The relatively thin layer of grey matter lining the sulci (Fig. 2) may limit CSD spread across this region, thereby accounting for the reduction in the number of events in the marginal gyrus (James et al. 1999). This adoption of imaging planes gave relatively homogeneous brain images that were confined to restricted brain gyri with clear tissue boundaries. The latter features facilitated the final mapping of DW–EPI results onto anatomical images.

Having defined the cerebral architecture, and determined the requisite investigative image plane, it was necessary then to define conditions of data acquisition in order to achieve series of images that had an acceptable temporal and spatial resolution. The alternate high-b and low-b scans were timed at intervals close to the highest sampling frequency permitted by our imaging hardware. A sufficient number of frames were obtained in order to encompass the secondary CSD episodes in their entirety. This entailed sampling periods that were substantially longer ($\sim$90 min) than used hitherto (previous maximum 16 min) (Gardner-Medwin et al. 1994; Latour et al. 1994; de Crespigny et al. 1998).

To investigate in detail the resulting CSD events within single frames (Figs 6, 7), either signal analysis or statistical methods of image processing were required. Thus unprocessed high-b DW-EPI frames assembled into movies convincingly revealed waves of altered diffusive properties spreading across the cortical surface but these were not readily amenable to quantification. An initial analytical approach subtracted a preresponse high-b image from the remaining post-KCl high-b images, followed by median-filtering and thresholding and superimposing onto a reference image. A second, more objective approach derived ADC values from consecutive pairs of low-b and high-b images. Running t tests then detected pixels with significantly different, more negative, ADC values. Both image analysis methods made it possible to visualise CSD wavefronts in stationary frames and offered generally concordant results. The latter procedure, however, provided more objective criteria for mapping and detection on the basis of absolute values of ADC, and more effectively detected and displayed the features and spatial spread of secondary waves (Fig. 7).

The final experiments investigated the appropriate methods for initiating CSD events under imaging conditions. Thus a CSD response that depends upon sustained KCl application that may diffuse someway across the cortical surface may differ from that induced by a shorter and potentially more localised application of KCl-saturated agar. Both protocols elicited qualitatively similar CSD responses (Fig. 8), in several animals, consistent with CSD having a regenerative cellular basis.

These studies have thus employed diffusion-weighted MRI to detect, reproducibly and unambiguously, successive waves of propagating change in cortical ADC in all animals studied so far. They provide preliminary, reproducible results and therefore the basis for further, detailed quantitative descriptions of CSD behaviour in the cat brain. Such studies should allow the magnitude, velocity and reproducibility of the ADC change between events and animals to be studied. They might thus form the basis of further investigations that could study the effects of anti-migraine compounds in future.

Quantitatively, our results showed that the ADC changes were confined to a single hemisphere and were most common in the gyrus where activity was

initiated, suggesting the presence of inhibitory boundaries that limit the spread of CSD activity in this gyrencephalic brain. The fact that grey matter thickness is not uniform across the cortex suggests that this may contribute to a physical boundary to CSD spread, although the physiological basis of this limitation remains to be determined. These findings in the cat brain suggest some minimum requirements that might be considered to detect and examine such changes in human studies of migraine. For example, aura is experienced in 10% of migraine patients who describe a classic 'slow march' of symptoms such as fortification spectra across the entire visual field. More common are less specific visual disturbances which again cover the full visual field and are seen in 25% of patients (Lance, 1993). It would be expected that in such subjects any associated CSD events might be located during the aura phase using fast, diffusion-weighted imaging targeted across the occipital cortex for 20–40 min to detect transient decreases in ADC. The techniques described here provide a possible means of directly detecting and analysing such CSD events. The necessary temporal resolution should be better than 2 high-b images per min with a 2.5×2.5 mm in-plane resolution and a 5 mm slice thickness. Migraine volunteers should ideally be imaged before and during the onset of a migraine episode. The routine detection of CSD might also be valuable in the management of stroke and head injury where recurrent PID events may well contribute to a favourable, or otherwise, outcome.

ACKNOWLEDGEMENTS

This research was supported by SmithKline Beecham Pharmaceuticals (M. F. J., M. I. S., A. A. P., K. H. J. B., J. M. S.), the Biotechnology and Biological Sciences Research Council (BBSRC), (N. G. P., C. L-H. H., D. P. B., T. A. C.), the University of Cambridge (J. M. S.) and the Herchel Smith Endowment (L. D. H., T. A. C.). C. L-H. H. is additionally grateful to the Medical Research Council (MRC) and the Royal Society for funding support.

REFERENCES

ANDERSON AW, GORE JC (1994) Analysis and correction of motion artefacts in diffusion weighted imaging. *Magnetic Resonance in Medicine* **32**, 379–387.

BACK T, KOHNO K, HOSSMANN KA (1994) Cortical negative DC deflections following middle cerebral artery occlusion and KCl-induced spreading depression: effect on blood flow, tissue oxygenation, and electroencephalogram. *Journal of Cerebral Blood Flow and Metabolism* **14**, 12–9.

BASSER PJ, MATTIELLO J, LE BIHAN D (1994) MR diffusion tensor spectroscopy and imaging. *Biophysical Journal* **66**, 259–267.

BASSER PJ, PIERPAOLI C (1996) Microstructural and physiological features of tissues elucidated by quantitative diffusion tensor MRI. *Journal of Magnetic Resonance Series B* **111**, 209–219.

BERMAN AL, JONES EG (1982) The thalamus and basal telencephalon of the cat: a cytoarchitectonic atlas with stereotaxic coordinates. Madison, WI: University of Wisconsin Press.

BURES J, BURESOVA O, KRIVANEK J (1974) *The Mechanisms and Applications of Leao's Spreading Depression of Electroencephalographic Activity*. New York: Wiley.

CROUCH JE (1969) *Text-atlas of Cat Anatomy*. Philadelphia: Lea and Febiger.

DE CRESPIGNY A, ROTHER J, VAN BRUGGEN N, BEAULIEU C, MOSELEY ME (1998) Magnetic resonance imaging assessment of cerebral hemodynamics during spreading depression in rats. *Journal of Cerebral Blood Flow and Metabolism* **18**, 1008–1117.

GARDNER-MEDWIN AR (1981) Possible roles of verebrate neuroglia in potassium dynamics, spreading depression and migraine. *Journal of Experimental Biology* **95**, 111–127.

GARDNER-MEDWIN AR, VAN BRUGGEN N, WILLIAMS SR, AHIER RG (1994) Magnetic resonance imaging of propagating waves of spreading depression in the anaesthetised rat. *Journal of Cerebral Blood Flow and Metabolism* **14**, 7–11.

HASEGAWA Y, LATOUR LL, FORMATO JE, SOTAK CH, FISHER M (1995) Spreading waves of a reduced diffusion coefficient of water in normal and ischemic rat brain. *Journal of Cerebral Blood Flow and Metabolism* **15**, 179–87.

HIGASHIDA H, MITARAI G, WATANABE S (1974) A comparative study of membrane potential changes in neurons and neuroglial cells during spreading depression in the rabbit. *Brain Research* **65**, 411–25.

HOSSMANN KA (1996) Periinfarct depolarizations. *Cerebrovasculature and Brain Metabolism Reviews* **8**, 195–208.

JAMES MF, SMITH MI, BOCKHORST KHJ, HALL LD, HOUSTON GC, PAPADAKIS NG et al. (1999) Cortical spreading depression in the gyrencephalic feline brain studied by magnetic resonance imaging. *Journal of Physiology* **519.2**, 415–425.

LANCE JW (1993) Current concepts of migraine pathogenesis. *Neurology* **43**, S11–5.

LARGO C, IBARZ JM, HERRERAS O (1997) Effects of the gliotoxin fluorocitrate on spreading depression and glial membrane potential in rat brain in situ. *Journal of Neurophysiology* **78**, 295–307.

LATOUR LL, HASEGAWA Y, FORMATO JE, FISHER M, SOTAK CH (1994) Spreading waves of decreased diffusion coefficient after cortical stimulation in the rat brain. *Magnetic Resonance in Medicine* **32**, 189–98.

LAURITZEN M (1994) Pathophysiology of the migraine aura. The spreading depression theory. *Brain* **117**, 199–210.

LEAO AAP, MORRISON RS (1945) Propagation of spreading cortical depression. *Journal of Neurophysiology* **8**, 33–45.

MANTZ J, CORDIER J, GIAUME C (1993) Effects of general anesthetics on intercellular communications mediated by gap junctions between astrocytes in primary culture. *Anesthesiology* **78**, 892–901.

MARSHALL WH (1959) Spreading cortical depression of Leao. *Physiological Reviews* **39**, 239–279.

MATIELLO J, BASSER PJ, LE BIHAN D (1997) The b matrix in diffusion tensor echo-planar imaging. *Magnetic Resonance in Medicine* **37**, 292–300.

MAYEVSKY A, DORON A, MANOR T, MEILIN S, ZARCHIN N, OUAKNINE GE (1996) Cortical spreading depression recorded from the human brain using a multiparametric monitoring system. *Brain Research* **740**, 268–74.

NICHOLSON C, KRAIG RP (1981) The behavior of extracellular ions during spreading depression. In *The Application of Ion-selective Microelectrodes* (ed. Zeuthen T). Amsterdam: Elsevier/North Holland Biomedical Press.

OCHS S, HUNT K (1960) Apical dendrites and propagation of spreading depression in cerebral cortex. *Journal of Neurophysiology* **23**, 434–444.

PAPADAKIS NG, XING D, HUANG CL-H, HALL LD, CARPENTER TA (1999) A comparative study of acquisition schemes for diffusion tensor imaging using MRI. *Journal of Magnetic Resonance* **137**, 67–82.

PIPER RD, LAMBERT GA (1996) Inhalational anesthetics inhibit spreading depression: relevance to migraine. *Cephalalgia* **16**, 87–92.

PRESS WH, FLANNERY BP, TEUKOLSKY SA, VETTERLING WT (1992) *The Art of Scientific Computing. Numerical Recipes in C*. Cambridge: Cambridge University Press.

READ SJ, SMITH MI, BENHAM CD, HUNTER AJ, PARSONS AA (1997) Furosemide inhibits regenerative cortical spreading depression in anaesthetized cats. *Cephalalgia* **17**, 826–32.

ROTHER J, DE CRESPIGNY AJ, D'ARCEUIL H, MOSLEY ME (1996) MR detection of cortical spreading depression immediately after focal ischemia in the rat. *Journal of Cerebral Blood Flow and Metabolism* **16**, 214–20.

SAITO R, GRAF R, HUBEL K, TAGUCHI J, ROSNER G, FUJITA T et al. (1995) Halothane, but not alpha-chloralose, blocks potassium-evoked cortical spreading depression in cats. *Brain Research* **699**, 109–15.

SNIDER RS, NIEMER WS (1970) *A Stereotaxic Atlas of the Cat Brain*. Chicago: University of Chicago Press.

SRAMKA M, BROZEK G, BURES J, NADVORNIK P (1977) Functional ablation by spreading depression: possible use in human stereotactic neurosurgery. *Applied Neurophysiology* **40**, 48–61.

SZERB JC (1991) Glutamate release and spreading depression in the fascia dentata in response to microdialysis with high K^+: role of glia. *Brain Research* **542**, 259–65.

TOWER DB, YOUNG OM (1973) The activities of butyryl-cholinesterase and carbonic anhydrase, the rate of anaerobic glycolysis, and the question of a constant density of glial cells in cerebral cortices of various mamalian species from mouse to whale. *Journal of Neurochemistry* **20**, 269–278.

TURNER R, LE BIHAN D, MAIER J, VAVREK R, HEDGES LK, PEKAR J (1990) Echo planar imaging of intravoxel incoherent motion. *Radiology* **177**, 407–414.

WEBB P, MACOVSKI A (1990) Rapid, fully automatic, arbitary volume in vivo shimming. *Magnetic Resonance in Medicine* **20**, 113–122.

XING D, PAPADAKIS NG, HUANG CL-H, LEE VM, CARPENTER TA, HALL LD (1997) Optimised diffusion-weighting for measurement of apparent diffusion coefficient (ADC) in human brain. *Magnetic Resonance Imaging* **15**, 771–84.